



<b>Publication Year</b>	2015
<b>Acceptance in OA</b>	2020-03-27T16:05:37Z
<b>Title</b>	Properties of barred spiral discs in hydrodynamical cosmological simulations
<b>Authors</b>	Goz, David, Monaco, Pierluigi, MURANTE, Giuseppe, CURIR, Anna
<b>Publisher's version (DOI)</b>	10.1093/mnras/stu2557
<b>Handle</b>	<a href="http://hdl.handle.net/20.500.12386/23645">http://hdl.handle.net/20.500.12386/23645</a>
<b>Journal</b>	MONTHLY NOTICES OF THE ROYAL ASTRONOMICAL SOCIETY
<b>Volume</b>	447

# Properties of barred spiral discs in hydrodynamical cosmological simulations

David Goz,<sup>1★</sup> Pierluigi Monaco,<sup>1,2</sup> Giuseppe Murante<sup>2</sup> and Anna Curir<sup>3</sup>

<sup>1</sup>*Dipartimento di Fisica - Sezione di Astronomia, Università di Trieste, via Tiepolo 11, I-34131 Trieste, Italy*

<sup>2</sup>*INAF, Osservatorio Astronomico di Trieste, Via Tiepolo 11, I-34131 Trieste, Italy*

<sup>3</sup>*INAF, Osservatorio Astronomico di Torino, Strada Osservatorio 20, I-10025 Pino Torinese, Italy*

Accepted 2014 December 2. Received 2014 November 6; in original form 2014 September 2

## ABSTRACT

We present a quantification of the properties of bars in two  $N$ -body+ smoothed particle hydrodynamics cosmological simulations of spiral galaxies, named GA and AqC. The initial conditions were obtained using the zoom-in technique and represent two dark matter haloes of  $2\text{--}3 \times 10^{12} M_{\odot}$ , available at two different resolutions. The resulting galaxies are presented in the companion paper of Murante et al. We find that the GA galaxy has a bar of length 8.8 kpc, present at the two resolution levels even though with a slightly different strength. Classical bar signatures (e.g. pattern of streaming motions, high  $m = 2$  Fourier mode with roughly constant phase) are consistently found at both resolutions. Though a close encounter with a merging satellite at  $z \sim 0.6$  (mass ratio 1: 50) causes a strong, transient spiral pattern and some heating of the disc, we find that bar instability is due to secular process, caused by a low Toomre parameter  $Q \lesssim 1$  due to accumulation of mass in the disc. The AqC galaxy has a slightly different history: it suffers a similar tidal disturbance due to a merging satellite at  $z \sim 0.5$  but with a mass ratio of 1: 32, that triggers a bar in the high-resolution simulation, while at low resolution the merging is found to take place at a later time, so that both secular evolution and merging are plausible triggers for bar instability.

**Key words:** methods: numerical – galaxies: formation – galaxies: kinematics and dynamics – galaxies: structure.

## 1 INTRODUCTION

The formation and evolution of structures within the Lambda cold dark matter cosmological model is a very active and quickly evolving field. In this cosmological framework, galaxies form through cooling and condensation of baryons within dark matter (DM) haloes (e.g. White & Rees 1978; Fall & Efstathiou 1980). The initial conditions are provided by cosmology, but the level of complexity of the problem is so high that following the evolution of galaxies is a great challenge. It is then convenient to address the problem using  $N$ -body hydrodynamical simulations. State-of-the-art hydrodynamical codes for the formation of galaxies include a treatment of the processes of radiative cooling, star formation, energy feedback from massive or dying stars, their chemical enrichment and, in some cases, accretion on to black holes and feedback from the resulting active galactic nuclei. Many of these processes take place on very small scales, compared with those that can be resolved by the simulation, so it is necessary to include them through suitable subresolution models. Thanks to recent progress, simulations

are now able to produce galaxies with realistic morphologies, sizes and gas fractions. In particular, despite the relatively unsuccessful simulations shown in the Aquila comparison project (Scannapieco et al. 2012), the challenge of producing a disc galaxy in a Milky Way-sized halo with quiet merging history has been successfully carried out by several groups (e.g. Governato et al. 2007; Guedes et al. 2011; Aumer et al. 2013; Marinacci, Pakmor & Springel 2013; Stinson et al. 2013).

One important observational aspect of disc galaxies is the presence of a bar: about 60 per cent of nearby disc galaxies are barred when observed in the near-infrared, while this figure lowers when galaxies are imaged in the optical (Eskridge et al. 2000; Barazza, Jogee & Marinova 2008). Bars are believed to play a key role in the secular evolution of galaxy discs, particularly in the redistribution of angular momentum of baryonic and DM components (Debattista & Sellwood 1996, 2000). The non-circular motions of bars cause the migration of gas within the corotation radius towards the galaxy centre, where it can give rise to a starburst or be accreted on a nuclear black hole. Also, the formation of a bar is believed to contribute to the formation of a discy or boxy/peanut bulge, often called pseudo-bulge (Kormendy 1982; Kormendy & Kennicutt 2004; Athanassoula 2005; Debattista et al. 2006).

\* E-mail: goz@oats.inaf.it

The emergence of bars in simulated galaxy discs has been addressed in many papers, starting from the pioneering work of Ostriker & Peebles (1973) where stability of a disc-shaped rotating  $N$ -body system was obtained only in the presence of an extended spherical halo. The origin of bars was ascribed to secular instabilities of massive discs (e.g. Efstathiou, Lake & Negroponte 1982) or to tidal interactions and merging with galaxy satellites, that excite spiral structures or proper bars (e.g. Noguchi 1996; Dubinski et al. 2008). Sellwood, Nelson & Tremaine (1998) noticed that disc stability is influenced by the presence of a soft or hard centre (namely a gently or steeply rising inner rotation curve), even when DM gives a negligible contribution to the inner part of the rotation curve.

More recent works addressed the effect of halo triaxiality (Curir & Mazzei 1999) and concentration (Athanasoula & Misiriotis 2002) on the growth of a bar in a disc hosted by an isolated halo with a Navarro, Frenk & White (1996) profile. In these works, the initial conditions represent an equilibrium configuration of a disc embedded in a DM halo; this setting is suitable to study bar formation in the absence of further external perturbations. Halo triaxiality was reported by Curir & Mazzei (1999) to be a trigger of bar formation, while Athanasoula & Misiriotis (2002) found that the bar strength correlates with halo concentration.

The study of bar formation in cosmological haloes has been faced in two ways. Curir, Mazzei & Murante (2006) built zoomed initial conditions (hereafter ICs) of DM haloes in cosmological volumes, let them evolve with an  $N$ -body code and placed model discs inside the haloes that were present at some specified redshift. That paper considered purely stellar discs, while stellar+gas discs were presented in Curir, Mazzei & Murante (2007), and the effect of star formation was considered in Curir, Mazzei & Murante (2008). In these works, it was shown that halo triaxiality, at the level commonly found in simulated DM haloes, triggers the formation of bars. The presence of gas leads to the destruction of the bar after a few dynamical times if the disc gas fraction is higher than  $\sim 20$  per cent, but the switching on of star formation inhibits this destruction. Different conclusions were reached by Berentzen, Shlosman & Jogee (2006), who noticed that the formation of a bar was weaker in haloes with higher triaxiality. Athanasoula, Machado & Rodionov (2013) showed the complex influence of halo triaxiality on the bar strength: at earlier times it triggers an instability while, at later times when secular evolution takes place, it has a stabilizing effect.

The second way of studying bar formation consists in addressing the emergence of bars in fully cosmological simulations of the formation of spiral galaxies (Kraljic, Bournaud & Martig 2012; Scannapieco & Athanasoula 2012; Guedes et al. 2013; Okamoto 2013; Okamoto, Isoe & Habe 2014). The obvious advantage of this approach, of a much more realistic representation of gravitational forces within a non-idealized DM halo, is balanced by the difficulty in obtaining a realistic disc galaxy in this context. In particular, extended discs with flat rotation curves are obtained only when efficient feedback from star formation is present, but too strong feedback can lead to the destruction of the disc (Scannapieco et al. 2012). This is where the subresolution modelling of stellar feedback becomes crucial.

Scannapieco & Athanasoula (2012), using the version of GADGET (Springel 2005) described in Scannapieco et al. (2006), found long and strong bars in two simulated galaxies; in particular the strengths, lengths and projected density profiles of the bars were found within the range of values given in the observations of Gadotti (2011). Kraljic et al. (2012), using the Eulerian code RAMSES (Teyssier 2002), studied the evolution of galactic bars in a sample of 33 zoomed-in cosmological haloes. They found that after  $z \approx 1$  almost 80 per cent

of spirals galaxies host bars, and they suggested that the epoch of bar formation starts from the late ‘secular’ phase and contributes to the growth of pseudo-bulges, even if the bulge mass budget remains dominated by the contribution of mergers. Furthermore, most of the bars formed at  $z \lesssim 1$  persists up to  $z = 0$ , while early bars at  $z > 1$  often disappear and reform several times. Okamoto (2013) analysed two simulations of disc galaxies with discy pseudo-bulges (Sérsic index  $< 2$ ), one of which presents a strong bar and a ‘boxy bulge’. They concluded that, at variance with the standard picture, the main channel of pseudo-bulge formation is high-redshift starbursts and not the secular evolution of the disc, although this contributes to it in a non-negligible way. Guedes et al. (2013) used their Eris simulation to investigate the interplay between a stellar bar and the formation and evolution of a pseudo-bulge. They found, again at variance with the standard picture, that the bulk of mass in their pseudo-bulge forms early ( $z \sim 4$ ), fast ( $\sim 2$  Gyr) and *in situ*, starting from a bar instability triggered by tidal interactions with a passing satellite. The bar is destroyed ( $z \sim 3$ ) by several minor mergers, then reforms later ( $z \sim 2$ ), again triggered by tidal interactions, but the redistribution of angular momentum within stars and gas, driven to the centre by the bar itself at  $z \sim 1$ , leads to the gradual breakup of the bar structure. Very recently, Okamoto et al. (2014) studied the evolution of two bars formed in cosmological Milky Way-sized haloes. As commonly found in idealized simulations, the rotation speed of the stronger bar was found to decrease with time by transferring its angular momentum to the DM halo, while other behaviours, such as oscillations of pattern speed, were more peculiar to the cosmological case. The weaker bar was found to slow down, while its amplitude was staying constant. The authors pointed out that the main difference between idealized and cosmological simulations is the inclusion of energy and mass released from stellar populations, which leads to a different central density structure.

In Murante et al. (2015) (hereafter Paper I), we present simulations of Milky Way-sized DM haloes performed with the Tree-PM+smoothed particle hydrodynamics (SPH) code GADGET3 (Springel 2005), where star formation and stellar feedback are treated with the subresolution model, named MULTi-Phase Particle Integrator (hereafter MUPPI), presented in Murante et al. (2010). These simulations follow the chemical enrichment of the interstellar medium (ISM) and its metal-dependent radiative cooling using the model of Tornatore et al. (2007) and Wiersma et al. (2009). The two sets of ICs for the simulations, the GA set by Stoehr et al. (2002) and the AqC set of Scannapieco et al. (2006), are available at different refinement levels, and they were used to study the stability of results with resolution. The resulting galaxies are shown in Paper I to resemble observed spirals in many regards; in particular, the resulting discs are extended, with small bulges ( $B/T \sim 0.2$ ) and flat rotation curves. As shown in that paper, at  $z = 0$  both spiral galaxies hosted by the two haloes show an extended bar and this feature is clearly visible at two resolutions both in GA and AqC sets.

In this paper, we quantify the properties and kinematics of the bars of the GA and AqC galaxies of Paper I. We find that, in the GA case and during the development of the instability ( $z \leq 0.3$ ), bar properties and time evolution are very similar at the two resolutions, while in the AqC case some differences are noticed that can be ascribed to the different orbits and timing of a minor merger at the two resolutions.

This is, to our knowledge, the first time that, in a cosmological simulation, a bar instability is found to develop in such a similar way at different resolutions. This prompts us to consider these bars as due to physical and not to numerical processes and to study the

**Table 1.** Basic characteristics of the different simulations. Column 1: simulation name; column 2: Plummer-equivalent softening length for gravitational forces, fixed in physical coordinates below  $z = 6$  and in comoving coordinates at higher redshift; column 3: mass of the gas particles; column 4: mass of the star particles; column 5: number of star particles within  $r_{200}/10$ ; column 6: virial radius  $r_{200}/10$ ; column 7: stellar bulge mass at  $z = 0$ ; column 8: stellar disc mass at  $z = 0$ ; column 9: bulge-over-total stellar mass ratio at  $z = 0$ ;

Simulation	$\epsilon_{\text{pl}}$ (kpc $h^{-1}$ )	$M_{\text{gas}}$ ( $M_{\odot} h^{-1}$ )	$M_{\text{star}}$ ( $M_{\odot} h^{-1}$ )	$N_{\text{star}}$	$r_{200}/10$ (kpc)	$M_{\text{bulge}}$ ( $M_{\odot}$ )	$M_{\text{disc}}$ ( $M_{\odot}$ )	$B/T$
GA2	0.325	$3.0 \times 10^5$	$7.5 \times 10^4$	1154 243	29.98	$1.4 \times 10^{10}$	$8.8 \times 10^{10}$	0.20
GA1	0.65	$2.8 \times 10^6$	$7.0 \times 10^5$	146 196	30.37	$2.0 \times 10^{10}$	$1.1 \times 10^{11}$	0.22
AqC5	0.325	$3.0 \times 10^5$	$7.5 \times 10^4$	803 889	23.82	$1.1 \times 10^{10}$	$5.7 \times 10^{10}$	0.23
AqC6	0.65	$2.4 \times 10^6$	$6.0 \times 10^5$	111 989	24.15	$1.4 \times 10^{10}$	$6.3 \times 10^{10}$	0.24

trigger of this instability, investigating the role of secular evolution and minor mergers.

The paper is organized as follows. Section 2 gives a brief account of the simulations used in this paper. Section 3 presents a complete quantification of stellar orbits and bar strength and length in the GA galaxies, addressing the question of the physical cause of the bar and the time at which it appears. Section 4 shows results for the AqC galaxies, highlighting the differences with the GA simulations and investigating the physical origin of such differences. Finally, Section 5 gives a summary and conclusions.

## 2 SIMULATIONS

Simulations were performed using the GADGET3 code (Springel 2005), where gravity is solved with a Tree code, aided by a particle mesh scheme at large scales, while hydrodynamics is integrated with an SPH solver that uses an explicitly entropy-conserving formulation with force symmetrization (Springel 2005). Star formation and feedback are performed with MUPPI (Murante et al. 2010), an effective model that attempts to take into account the structure of the ISM at unresolved scales by assuming that each gas particle, at sufficiently high density, is made up of a cold and a hot phase in thermal pressure equilibrium, plus a virtual stellar component. Energy from feedback is distributed to neighbouring particles both in the form of thermal and kinetic energy, as described in Paper I and in Murante et al. (2010). Chemical evolution and tracking of 11 elements is performed with the code of Tornatore et al. (2007), while metal-dependent cooling is performed following Wiersma et al. (2009). A full description of the code is given in the companion paper of Paper I; we refer to this paper for all details.

The two sets of ICs that we used are resimulations of DM haloes of mass  $\sim 3 \times 10^{12} M_{\odot}$  (GA) and  $\sim 2 \times 10^{12} M_{\odot}$  (AqC), with quiet merger history since  $z \sim 2$  so as to avoid the risk of late-time major mergers that can severely damage or destroy the discs. In particular, the AqC is part of the Aquarius series (Springel et al. 2008) of eight haloes, used by Scannapieco et al. (2009) to study the formation of disc galaxies; it was chosen because it was giving the lowest bulge-over-total ( $B/T$ ) ratio in that paper. Its level 6 and 5 resolutions were used in the Aquila comparison project (Scannapieco et al. 2012), in which we participated with an early version of our code with primordial cooling and purely thermal feedback. As a matter of fact, both galaxies happen to suffer a minor merger of mass ratio of the order of 1: 50 (GA) and 1: 30 (AqC) at  $z \sim 0.5$ . For both sets of ICs, we use two resolution levels with initial gas particle masses of  $\sim 2 \times 10^6 M_{\odot}$  (GA1 and AqC6) and  $\sim 3 \times 10^5 M_{\odot}$  (GA2 and AqC5). Plummer-equivalent softening at  $z < 6$  is set, for the two resolutions, to 0.65 and 0.325 kpc  $h^{-1}$  in physical coordinates, at higher redshift we keep it fixed in comoving coordinates.

Table 1 reports the main properties of the four sets of ICs, together with the main properties of their central galaxies at  $z = 0$ .

Simulations were post-processed with a standard friends-of-friends (FoF) algorithm to select the main halo of the high-resolution region and with the substructure-finding code SUBFIND (Springel et al. 2001). We assumed that the particles that constitute the galaxy are stars and cold ( $T < 10^5$  K) or multiphase gas particles, hereafter called ‘galaxy particles’. The galaxy was first identified as the object laying within  $1/10$  of the virial radius  $r_{200}$ , centred on the centre of mass of the FoF halo, and then the galaxy position was refined by computing the centre of mass of galaxy particles lying within 8 kpc (a distance at which it is unlikely to find satellite galaxies) and by iterating the computation with the new centre until convergence within 1 pc was reached. We checked that this position is very similar to the centre of the main substructure of the FoF halo, computed by SUBFIND using the position of the most bound particle. The reference frame was then aligned with the inertia tensor of galaxy particles, with the  $Z$ -axis<sup>1</sup> along the eigenvector corresponding to the largest eigenvalue and in the direction so as to have a positive scalar product with the angular momentum; the other two axes were aligned with the other eigenvectors so as to preserve the property  $\hat{X} \times \hat{Y} = \hat{Z}$ . We checked that, whenever a significant disc is present, the angular momentum of the galaxy particles within  $r_{200}/10$  is always very well aligned, within less than  $1^\circ$ , with the  $Z$ -axis.

## 3 THE GA1 AND GA2 GALAXIES

In this section, we study the GA galaxies obtained at the two resolution levels, GA1 (lower resolution) and GA2 (higher resolution). We show both simulations to address the stability of our result with respect to resolution.

### 3.1 The vertical structure of the disc

The relatively high values of the force softening used in these simulations do not allow us to resolve the vertical structure of the stellar thin disc. Nevertheless, the kinematic state of the disc is relevant in the study of disc instabilities, as it is well known that a hot disc is more stable (see e.g. the analysis based on the Toomre parameter presented below). From this point of view, it is a better choice to address the distribution of stellar velocities in place of stellar positions. Indeed, the force exerted by a planar distribution of mass depends mostly on its mass surface density, a quantity that is independent of disc scaleheight, so we expect the velocity dispersion of stars to be more convergent with resolution than the scaleheight itself. Below, we compute the velocity dispersion both in the vertical,  $Z$ -direction and in the radial,  $r$ -direction. The latter enters in the Toomre stability criterion.

<sup>1</sup> In this paper, we use the small letter  $z$  to denote redshift and the capital letter  $Z$  to denote the spatial vertical axis.

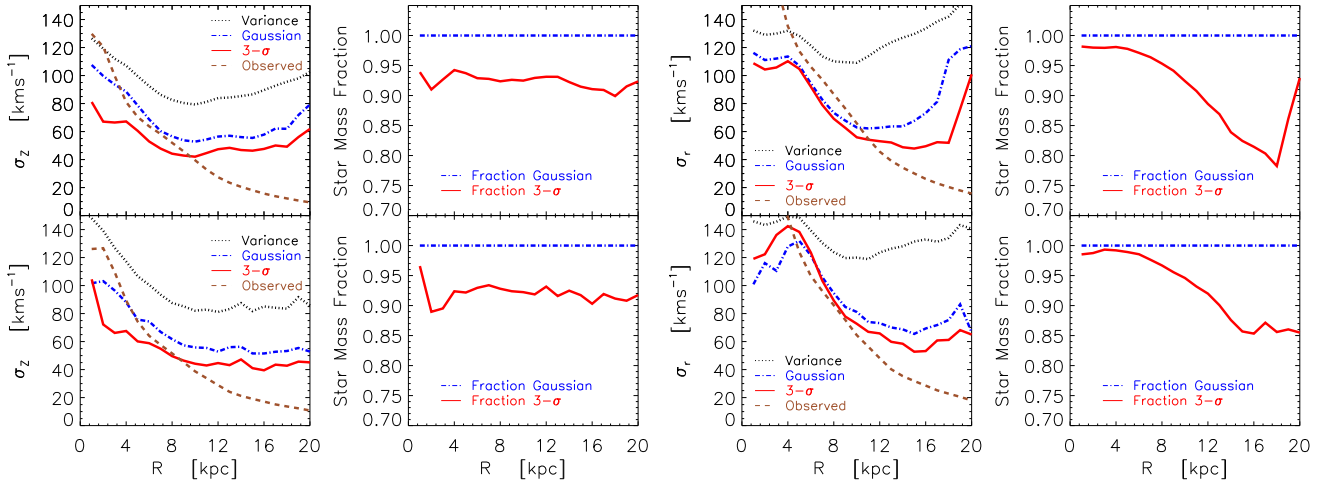


**Figure 1.** Vertical velocity dispersion  $\sigma_z$  and  $\sigma_r$ , and fractions of mass used to compute the relative dispersion; the variance and Gaussian fit methods use all particles, so for these the latter quantity is unity, while the  $3\sigma$  rejection method excludes particles with large velocities and in this case the latter quantity gives the fraction of mass that has not been excluded. The upper figures give results for GA2, the lower figures for GA1. The left pair of panels gives results for  $\sigma_z$ , the right pair for  $\sigma_r$ . Dotted black, dot-dashed blue, continuous red and dashed brown lines give respectively the rms, Gaussian,  $3\sigma$  rejection and observation-oriented estimates of velocity dispersion.

To compute stellar velocity dispersion, we use all stars within  $r_{200}/10$  from the centre, so at each polar radius we will have a mix of stars from the disc and from the stellar halo.<sup>2</sup> Assuming that the thin disc is the most massive component and that its vertical or radial velocities are roughly Gaussian distributed, the (mass-weighted) variance of disc stars will be severely affected by the minor component with a higher velocity dispersion. Fig. 1 shows, for both GA2 (upper panels) and GA1 (lower panels), the mass-weighted root mean square (hereafter rms) of vertical (left-hand panels) and radial (right-hand panels) velocity dispersion of all stars as black lines. Fig. 2 reports, for the radial bin from 3 to 4 kpc, the mass-weighted histogram of vertical velocities in which black vertical lines mark the rms of the distribution, that is clearly not representative of the width of the main component.

To improve this measure, we tested two options: a Gaussian fit of the distribution of velocities in each bin of polar radius (blue lines in the two figures) and a Gaussian fit with recursive rejection of  $>3\sigma$  interlopers, performed until convergence is reached (red lines in the two figures). Since the  $3\sigma$  rejection method implies that some mass is discarded, in Fig. 1 we report on the right of velocity profiles the fraction of mass that is used to compute them, as a function of radial distance. The Gaussian fit method uses all the mass, so it is reported as a line at unity. It can be noticed that, for both velocity components, the Gaussian fit method gives significantly lower velocity dispersion, while a further suppression is obtained with the  $3\sigma$  rejection method. The predicted distributions are shown in Fig. 2, again as blue and red lines. From this figure, it is apparent that the  $3\sigma$  rejection method gives the most faithful representation of the width of the main mass component, at the modest cost of excluding less than 10 percent of mass in the case of vertical velocity dispersion  $\sigma_z$  and an amount ranging from 1–2 percent at small radii to  $\sim 20$  percent at large distances in the case of the radial velocity dispersion  $\sigma_r$ . We also tried to fit the velocity

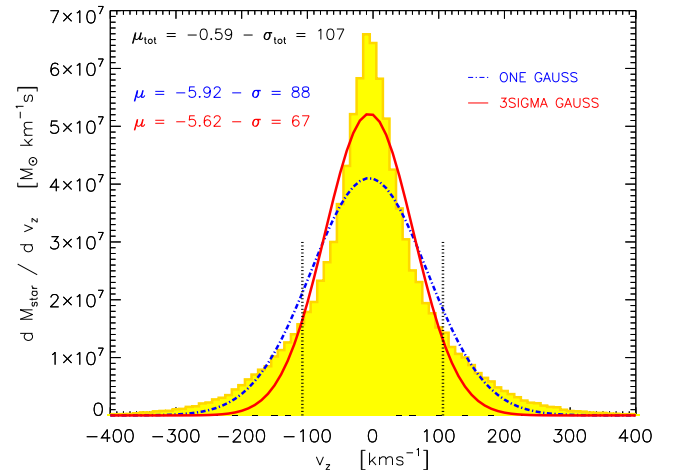


**Figure 2.** Mass-weighted histogram of stellar velocities for GA2 in the radial bin from 3 to 4 kpc for the GA2 galaxy at  $z = 0$ . Measured average and rms are  $\mu_{\text{tot}} = -0.59 \text{ km s}^{-1}$  and  $\sigma_{\text{tot}} = 107 \text{ km s}^{-1}$ , the rms is denoted by two dotted black vertical lines. The resulting fits (top left of the panel) for averages and dispersion with the Gaussian fit (dot-dashed blue line) and  $3\sigma$  rejection (continuous red line) methods are reported in the figure with the same colour as the corresponding line, in  $\text{km s}^{-1}$ .

distributions with two Gaussians, but the results were unstable and not satisfactory and for this reason we dropped this method.

In Fig. 1, we also compare these estimates of  $\sigma_z$  and  $\sigma_r$  with observation-oriented estimates. We follow Leroy et al. (2008), who computed the Toomre  $Q$  parameter for the THINGS (The HI Nearby Galaxy Survey) sample of local galaxies. Since direct measurements of stellar velocity dispersion are *extremely scarce*, in their appendix B they assumed that the stellar scaleheight  $h_*$  is constant throughout the disc, that this same quantity is related to the disc scale radius  $r_*$  through the observed relation  $h_* = r_*/7.3$  and that stars are isothermal in the  $Z$ -direction. As a result

$$\sigma_z = \sqrt{\Sigma_* \frac{2\pi G r_*}{7.3}}, \quad (1)$$

<sup>2</sup> We may have some contribution from a thick disc component, whose study is however hampered by the relatively poor softening that we use and is anyway beyond the interests of this paper.

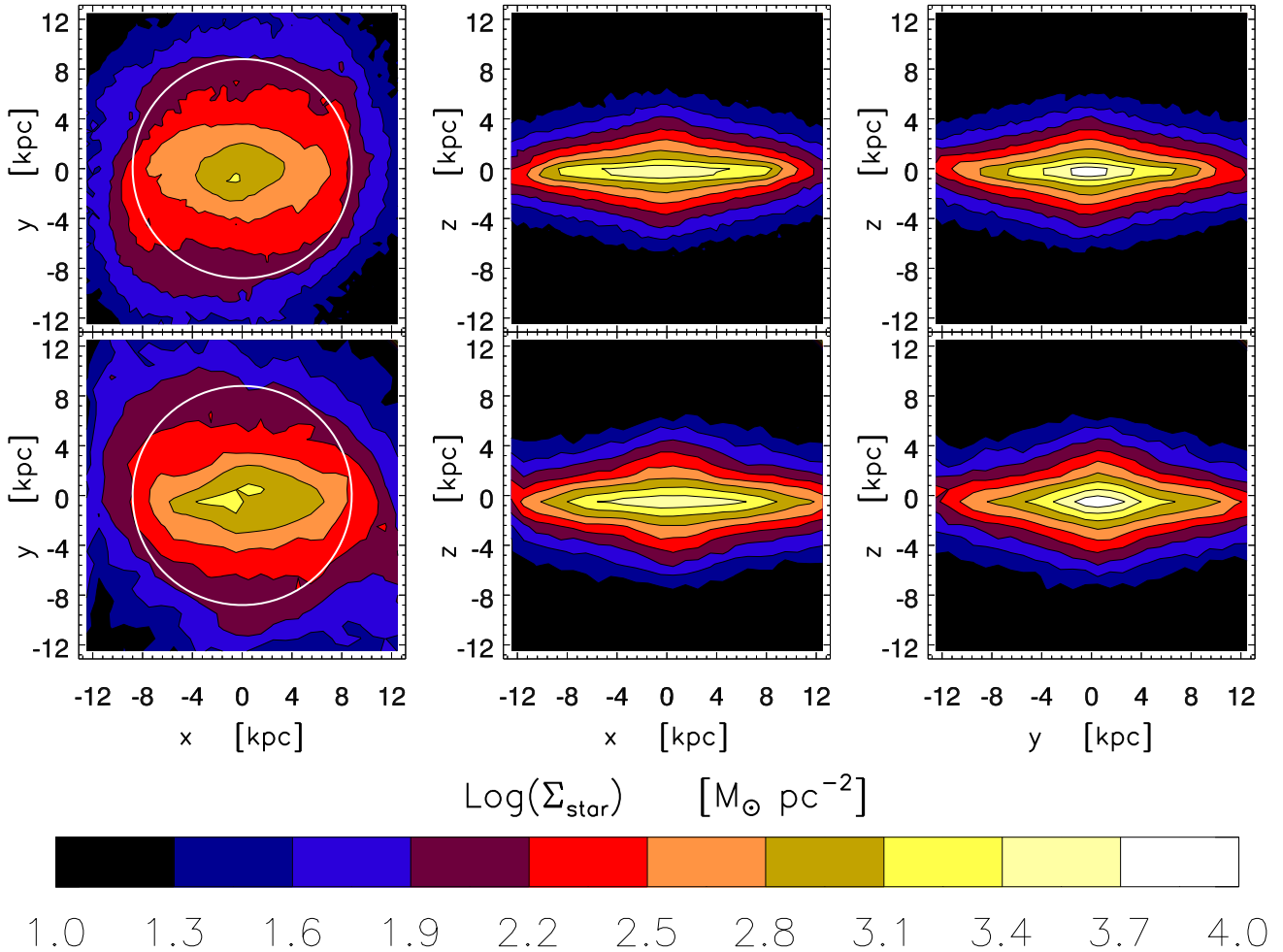


**Figure 3.** Projected stellar maps of the GA2 (upper panels) and GA1 (lower panels) galaxies at  $z = 0$  in boxes centred on the galaxy that extend 25 kpc across. Colour coding follows the log of stellar mass surface density as indicated by the colour bar. The three columns show projections in the face-on  $XY$ -plane (left), edge-on  $XZ$ -plane (middle) and edge-on  $YZ$ -plane (right). The white circle marks the bar length  $L_{\text{bar}}$ .

where  $\Sigma_*$  is the disc stellar surface density. For the radial velocity dispersion, the same authors assumed that  $0.6\sigma_r = \sigma_z$ . For the GA1 and GA2 discs, we use a disc scale-length  $r_* = 3.93$  and 4.45 kpc, estimated in Paper I by fitting the radial profile of stellar mass surface density. These estimates are shown in the Fig. 1 as brown lines. As a result, at  $r < 10$  kpc both the Gaussian and the  $3\sigma$  rejection methods yield velocity dispersions that are broadly compatible with those that would be expected in an observed galaxy. In more detail, GA1 shows a marginally hotter disc, especially as far as radial motions are concerned, but these are influenced by the radial streaming motions due to the bar itself, that will be quantified below. The outer parts of the disc are significantly hotter than this estimate, but we know that, at large distances, disc scale-lengths start to increase, so this discrepancy could be not very significant.

This analysis demonstrates that, despite the relatively large softenings used, the kinematic state of our discs is compatible with observational evidence, at least in the inner regions that are subject to bar instability. However, we know that these velocity dispersions are severely affected by numerics and the marginally hotter GA1 disc clearly supports this warning. In Paper I, we present results of simulations of the GA1 obtained with different softenings and we show that, while lower values of the softening result in higher stellar velocity dispersion (simply measured there as rms), con-

vergence is not yet fully achieved for the value of softening used here. Therefore, these velocities are very likely influenced by two-body scattering of star particles, but this influence does not lead to unrealistic thickening of the disc.

### 3.2 Morphology and circularities

Extended density maps of the two galaxies are given in Paper I. Fig. 3 shows maps of stellar mass surface density for the central part of the two simulated galaxies at redshift 0. Each map spans  $\pm 12.5$  kpc in each dimension. The figure shows, on the upper panels, the maps of the GA2 simulation in the  $XY$ -,  $XZ$ - and  $YZ$ -plane, while the lower panels show the same maps for the GA1 simulation. The colour coding represents the log surface density, and values are given in the colour bar. The maps were obtained by projecting all star particles within  $r_{200}/10$  and smoothing the resulting surface densities on a grid, whose pixel is set equal to the softening length in both cases. We find that in both simulations the isodensity contours in the face-on map are not round but present a flattened structure; the bar is aligned along the  $X$ -axis. The edge-on maps sample the bar along its long ( $XZ$  projection) and short ( $YZ$  projection) axes and, as expected, the isodensity contours are flatter when the disc particle distribution is seen along the major bar axis.

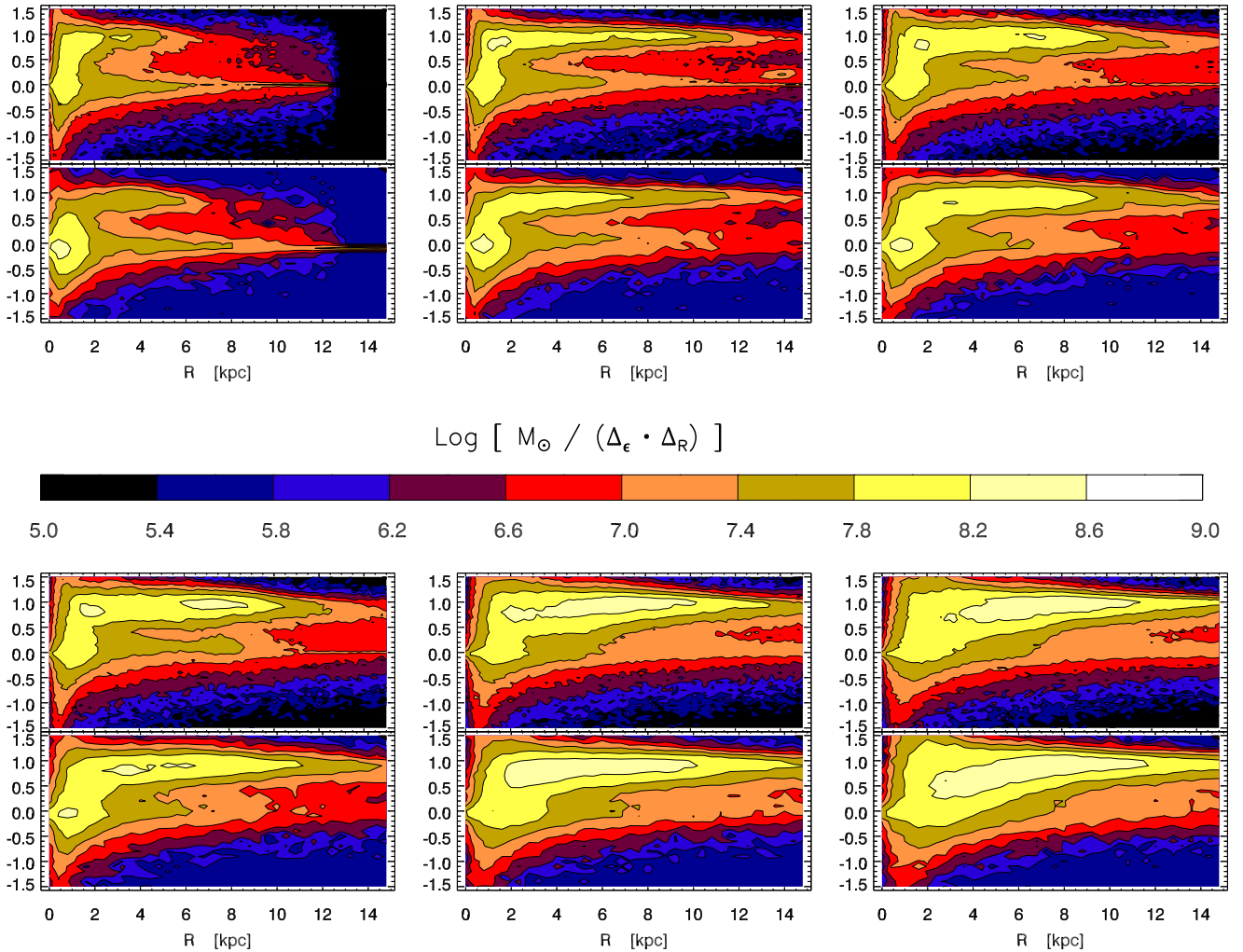


**Figure 4.** 2D histograms of circularity (equation 2) and polar radius, at six different times. In each panel, colour coding refers to the log of stellar mass per unit bin area as indicated by the colour bar, the black lines are the corresponding isodensity contours. Each pair of panels gives results for the GA2 (upper panels) and GA1 (lower panels) galaxies. From the upper-left panels, redshifts are  $z = 1.5, 1, 0.7, 0.5, 0.2, 0$ .

The circularity of a star particle is usually defined as the ratio of the  $z$ -component of its specific angular momentum,  $j_z = rv_{\text{tan}}$  (where  $v_{\text{tan}}$  is the tangential velocity in a cylindrical coordinate system) to the angular momentum of a reference circular orbit. Two methods have been proposed to compute this reference angular momentum. Scannapieco et al. (2009) and other authors used the angular momentum of a circular orbit at the same radius,  $j_{\text{circ}} = r\sqrt{GM(<r)}/r$ , while Abadi et al. (2003) proposed to use  $J_{\text{max}}(E)$ , the maximum specific angular momentum possible given the binding energy of the particle  $E$ . This second definition constrains circularity to be  $< 1$ . As in Paper I, in this paper we use the first definition, so that

$$\epsilon = j_z / j_{\text{circ}}. \quad (2)$$

However, we also tested the second definition at  $z = 0$  and found the same qualitative features of the circularity diagrams obtained with equation (2).

In Fig. 4, we show 2D histograms of circularities as a function of polar radius  $r$  along the galaxy discs, for both galaxies at six different times. We expect a disc to be visible as a narrow distribution around  $\epsilon \sim 1$ , while a component scattering around  $\epsilon \sim 0$  will be identified as a bulge or a spherical halo, depending on  $r$ . The 2D histograms are shown as a map of mass per unit bin size (kpc and circularity in the

two dimensions), with isodensity contours showing the preferential locus of star particles. For each row, the upper and lower panels give the histogram for GA2 and GA1, respectively. Starting from the upper-left panels, the two rows show results for  $z = 1.5, 1, 0.7, 0.5, 0.2, 0$ . These times are chosen to follow the main phases of the formation of the bar, as it will be explained below. This figure allows us to monitor the formation of the disc in the two simulations. The first point that is worth noting is that the circularity histograms are notably independent of resolution, so we will describe GA1 and GA2 together. At  $z = 1.5$ , the galaxy is mostly a spheroid, while a disc has started to form at  $r < 6$  kpc. A clear and thin disc structure is visible at  $z = 1$ . The structure is broader at  $z < 0.6$ , where tidal interactions with a satellite of mass  $M_* = 1.2 \times 10^9 M_\odot$ , that culminate with a minor merger at  $z = 0.35$ , are heating the disc. Beyond  $z = 0.2$ , the region at intermediate circularities,  $\epsilon \sim 0.5$  and at  $1 < r < 5$  kpc, starts to be populated, especially for the GA1 galaxy. Because stars in the bar have large systematic radial motions, this is a sign of the emergence of a bar structure.

The fraction of stellar mass as a function of circularity, i.e. the projection in radius of the circularity histograms of Fig. 4, is shown in fig. 3 of Paper I for  $z = 0$ . There a simple, kinematically based decomposition (that loosely follows Scannapieco et al. 2008) is

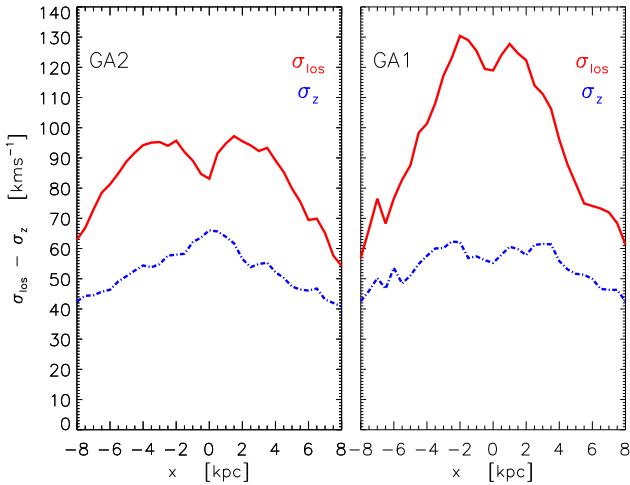


**Figure 5.** Profiles of line-of-sight velocity dispersion  $\sigma_{\text{los}}$  (continuous red lines) and vertical velocity dispersion  $\sigma_z$  (dot-dashed blue lines) of stars at  $z = 0$ , when the galaxy is observed edge-on in the direction perpendicular to the bar main axis. Left- and right-hand panels show GA2 and GA1.

used to compute the stellar  $B/T$ . We assume that counter-rotating star particles ( $\epsilon < 0$ ) within  $r_{200}/10$  constitute half of the spheroidal component, so the bulge mass is computed as twice the mass of these counter-rotating stars.  $B/T$  was then computed as

$$B/T = M_{\text{bulge}} / (M_{\text{bulge}} + M_{\text{disc}}) \quad (3)$$

$B/T$  values at  $z = 0$  are reported in Table 1.

### 3.3 Kinematics of the central region

Here, we quantify the kinematics of the central region of the galaxy, that hosts both bar and bulge. It will be demonstrated in Section 3.5 that in GA1 as well as in GA2 a bar appears only towards the end of the simulation, starting from  $z = 0.2$ , so we analyse here only the galaxy at  $z = 0$ .

As suggested by Okamoto (2013), the expected kinematic signature of a bar is a higher value of line-of-sight velocities with respect to vertical ones. We repeat the analysis suggested in that paper in Fig. 5, that shows velocity dispersion  $\sigma_{\text{los}}$  of stars along the ‘line of sight’ (the  $Y$ -axis in the density maps; red lines in the figure) and along the vertical direction  $\sigma_z$  ( $Z$ -axis; blue lines in the figure). Velocity dispersions were computed with the  $3\sigma$  rejection method explained in Section 3.1.

We find that while vertical velocity dispersion gets values of  $\sim 50\text{--}60 \text{ km s}^{-1}$  with a very flat dependence on distance from the centre, radial velocity dispersion takes higher values. In the GA2 case, radial velocities peak at  $\sim 100 \text{ km s}^{-1}$ , twice the vertical ones, while in the GA1 case an even higher peak ( $130 \text{ km s}^{-1}$ ) is present. In both cases, a small dip at the galaxy centre is present.

A pronounced, radial streaming pattern is expected in non-axisymmetric potentials like that of a stellar bar (e.g. Bosma 1978). Fig. 6 shows 2D maps, in the face-on  $XY$  plane, of average radial velocities computed on the same box size and grid as in Fig. 3. To minimize contamination from halo motions, median velocities are computed only for stars lying within 1 kpc from the midplane. As shown in the colour bar below, blue/black colours denote negative velocities, while yellow/white colours denote positive velocities. A symmetric and squared pattern of streaming motions is evident in both cases, with higher velocities for the GA1 galaxy. At larger distances from the centre, the velocity pattern connected to the spiral

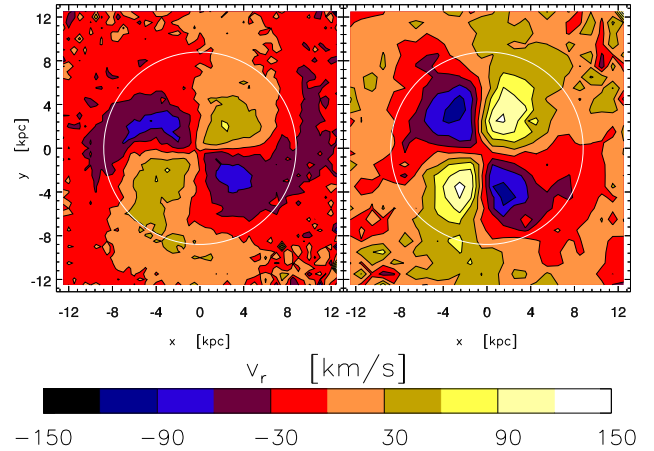


**Figure 6.** Radial velocity maps on face-on views ( $XY$  projection) of the two simulated GA2 (left-hand panel) and GA1 (right-hand panel) galaxies. The boxes are 25 kpc across. Colour coding follows the median radial velocity of stars within 1 kpc from the midplane, as indicated by the colour bar. The white circle marks the bar length  $L_{\text{bar}}$ .

arms is very visible for GA2. We conclude that the kinematics of stars in the inner regions of these galaxies is dominated by streaming motions as expected.

### 3.4 Quantification of bar strength and length

We quantify the strength of the bar following the analysis of Scannapieco & Athanassoula (2012) and Kraljic et al. (2012). This is based on the Fourier transform of the surface density of the disc:

$$\Sigma(r, \theta) = \frac{a_0(r)}{2} + \sum_{n=1}^{\infty} [a_n(r) \cos(n\theta) + b_n(r) \sin(n\theta)], \quad (4)$$

where  $r$  is the polar radius and  $\theta$  the azimuthal position on the disc plane. To perform the transform, particles are radially binned and the following coefficients are computed for each bin:

$$a_n(r) = \frac{1}{\pi} \int_0^{2\pi} \Sigma(r) \cos(n\theta) d\theta, \quad (n \geq 0) \quad (5)$$

$$b_n(r) = \frac{1}{\pi} \int_0^{2\pi} \Sigma(r) \sin(n\theta) d\theta, \quad (n > 0), \quad (6)$$

where  $\Sigma$  is the surface density of the stellar disc. The Fourier amplitude of each mode is defined as

$$C_n(r) = \sqrt{a_n^2(r) + b_n^2(r)}, \quad C_0(r) = a_0(r)/2. \quad (7)$$

The presence of a bar is revealed by a significant value of the  $C_2$  component, that is higher than even components of further order.

In Fig. 7, we show the amplitudes of the first four even components, normalized to the  $n = 0$  one,  $C_n/C_0$ . In both cases, the  $C_2$  component is significantly higher than the other components; for the GA2, it peaks at a value of 0.4 at 6 kpc, with a broad plateau starting from 2 kpc. GA1 shows a narrower plateau between 5 and 7 kpc, reaching a higher value of 0.7. This confirms that, consistently with the higher radial velocities, the bar in the GA1 simulation is stronger than in GA2. Higher order moments show smaller and smaller values in both cases; they peak at different scales and this is a sign that the bar is not perfectly symmetric. We also checked that odd modes have small values and this is again consistent with what we expect from a bar.

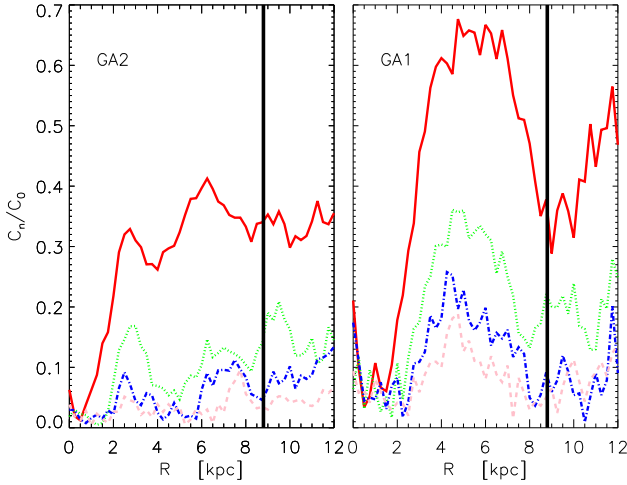


**Figure 7.** Fourier amplitudes  $C_n/C_0$  for even components  $n = 2$  (continuous red line),  $n = 4$  (dotted green line),  $n = 6$  (dot-dashed blue line),  $n = 8$  (dashed pink line) for stars of GA2 (left-hand panel) and GA1 (right-hand panel). The black lines mark the bar length  $L_{\text{bar}}$  kpc.

These results are broadly consistent with observations that show a variety of radial Fourier profiles of bars, ranging from simple symmetric profiles, that can be represented by two overlapping Gaussian components, to more complex curves. Since  $C_n/C_0$  value spans between 0.4 and 0.8 (Elmegreen & Elmegreen 1985; Ohta, Hamabe & Wakamatsu 1990; Ohta 1996; Aguerri, Beckman & Prieto 1998; Aguerri, Debattista & Corsini 2003; Buta et al. 2006), both GA galaxies would be classified as barred. Moreover, the amplitudes of GA2 show relatively high values also at large radii, where the signature of streaming motions (Fig. 6) is already lost but prominent spiral arms are present. This shows a limit of the analysis based simply on Fourier amplitudes, where spiral arms give weak signatures that can be confused with those of bars.

To evaluate the length of the bar, among many published methods (e.g. Combes & Elmegreen 1993; Debattista & Sellwood 2000; Michel-Dansac & Wozniak 2006), we use the one proposed by Athanassoula & Misiriotis (2002). This is based on the fact that, for an ideal bar, the phase of the  $m = 2$  mode should be constant as long as the probed scale is within the bar, while beyond it the phase is expected to fluctuate due to spiral arms. We implement this method by calculating, for each radial bin, the phase  $\Phi$  of the  $m = 2$  mode as

$$\Phi(r) = \arctan(b_2(r)/a_2(r)). \quad (8)$$

The average phase is computed applying equations (5) and (6) to all star particles with  $r < 12.5$  kpc, then computing  $\Phi_{\text{disc}}$  as in equation (8). The result is reported in Fig. 8 as a red line, while the green one corresponds to the average phase. The bar length is defined as the largest radius where these two last quantities differ less than a certain value. As discussed in Athanassoula & Misiriotis (2002), the choice of the constant is somehow arbitrary. In that paper, the authors suggested a range of  $\pm \arcsin(0.3)$ , while tighter ranges were used by other authors (e.g. Kraljic et al. 2012 used  $\pm \arcsin(0.1)$ ). We will demonstrate below that the GA2 bar is a caught in an early development phase and it is still weak, so we adopt the more permissive criterion of  $\pm \arcsin(0.3)$ . For both GA2 (left-hand panel) and GA1 (right-hand panel), the phase fluctuates in the inner 1–2 kpc, then is relatively stable for several kpc and goes out of the shaded region at 8.8 kpc in both cases. It must be noticed that the phase of GA2 gets marginally above the shaded region from

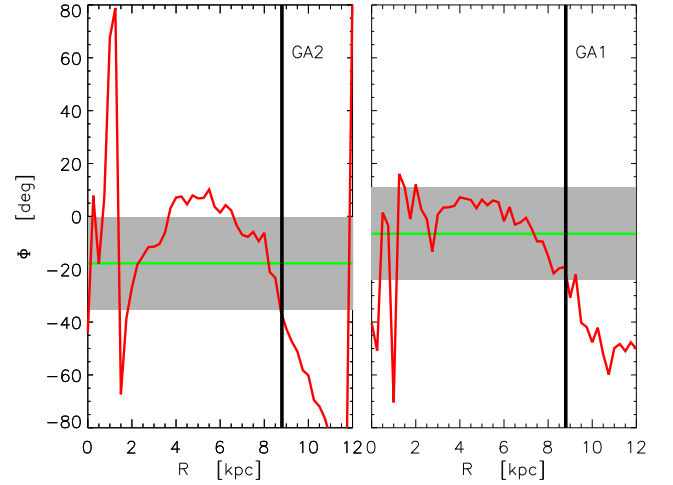


**Figure 8.** Phase of stellar distribution for GA2 (left-hand panel) and GA1 (right-hand panel). Red lines report the phase  $\Phi$  of the  $n = 2$  mode as a function of radius, the green horizontal line marks the overall phase  $\Phi_{\text{disc}}$  of the disc within 12.5 kpc. The shaded area gives the allowed range of  $\Phi_{\text{disc}} \pm \arcsin(0.3)$ . The black lines correspond to the bar length  $L_{\text{bar}}$ .

4 to 6 kpc, but given the arbitrariness of the used value we neglect this minor issue. We then take  $L_{\text{bar}} = 8.8$  kpc as a measure of bar length (see the vertical black line in the figure) and notice that it is remarkably independent of resolution.

Another possible method proposed by Athanassoula & Misiriotis (2002) to evaluate bar length is based on the scale at which the Fourier coefficient  $C_2/C_0$  goes to zero. Indeed, for an ideal bar on an axisymmetric disc, we would expect this coefficient to show a plateau and then drop quickly beyond the bar. In a more realistic context, one should define a threshold with respect to the maximum and define the bar length as the radius at which the amplitude of the Fourier mode gets below it. In Fig. 7, the vertical black lines denote the bar length as estimated by the phase method. In the GA1 case, using a drop of the coefficient by a factor of 2, it would give almost the same bar length, while, as noticed above, in the GA2 case the spiral pattern gives a signal comparable to that of the bar.  $L_{\text{bar}}$  is reported as a circle also in Figs 3 and 6 and in both cases the estimated bar length separates the inner region, dominated by flattened isodensity contours and streaming motions, from the outer region dominated by spiral arms. We conclude that the phase method gives a fair estimate of  $L_{\text{bar}}$ .

We can compare our results with  $\sim 300$  observed galaxies presented in Gadotti (2011); our  $L_{\text{bar}}$  value is at the high end of the distribution given in this observational work, but well compatible with it.

### 3.5 The origin of bar instability

To estimate the time at which the bar is triggered, we quantify how bar strength grows by computing the so-called relative mode strength  $A_2$ . This is the ratio of the integrals, weighted by area, of the coefficients  $C_2$  and  $C_0$  over the bar length  $L_{\text{bar}}$ , taking into account its value estimated by the previous method in Section 3.4.

$$A_2 = \frac{\int_0^{L_{\text{bar}}} C_2(R) R dR}{\int_0^{L_{\text{bar}}} C_0(R) R dR}. \quad (9)$$

We perform this calculation for all simulation outputs since  $z = 1$ , when the disc is still young and both GA1 and GA2 show no sign of a bar. Fig. 9 shows the evolution of  $A_2$  with redshift for GA2

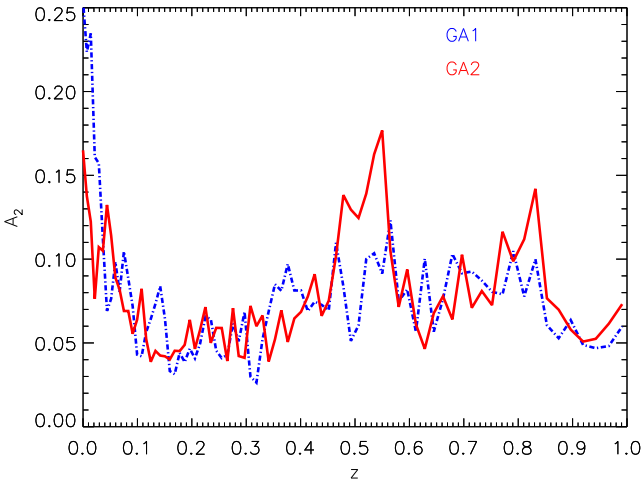


**Figure 9.** Relative mode strength  $A_2$  as a function of redshift for the GA1 (dot-dashed blue) and GA2 (continuous red) galaxies, starting from  $z = 1$ .

(red line) and GA1 (blue line). At  $z < 0.7$ , two different episodes of growth of  $A_2$  are visible at  $z$  from 0.6 to 0.45 (at least for GA2) and at  $z < 0.2$ . The episode at  $z \sim 0.5$  is due to a minor merger already mentioned above. A satellite of stellar mass  $1.25 \times 10^9 M_\odot$  in GA2 and  $1.35 \times 10^9 M_\odot$  in GA1 performs close orbits around the main galaxy. For GA2, the closest encounter is found at  $z = 0.57$ , where the distance of the satellite from the galaxy centre is 12 kpc. The stellar mass ratio is 1: 50 at the beginning of the interaction, slowly decreasing because of the continuous growth of the stellar mass of the central galaxy. Two more close encounters are found before the satellite is tidally disrupted into the halo of the main galaxy ( $z = 0.35$ ). These interactions trigger non-axisymmetric perturbations, so that GA2 acquires  $A_2$  values equivalent to those at  $z = 0$ . During this period, the disc is noticeably disturbed and a bar-like morphology is visible only in one output (the time interval between outputs being  $\sim 100$  Myr). In Fig. 10, we show in the left-hand panel a face-on density map of GA2 at  $z = 0.55$  (just after the nearest encounter), analogous to Fig. 3, and in the right-hand panels the  $C_2/C_0$  and phase diagrams, analogous to Figs 7 and 8. While disc morphology is clearly disturbed, the  $C_2$  coefficient

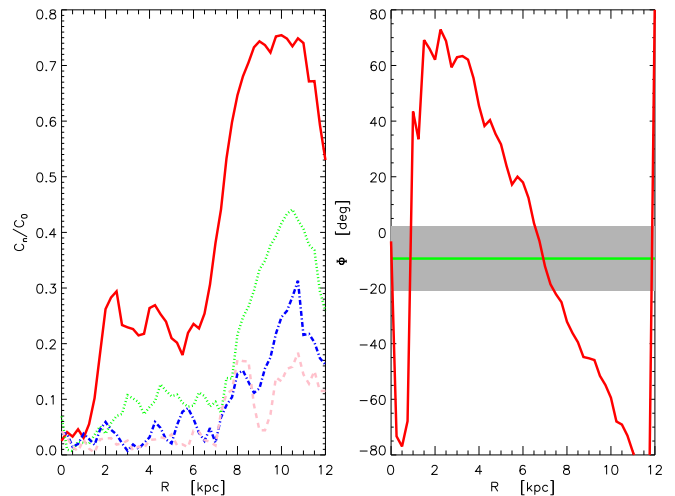
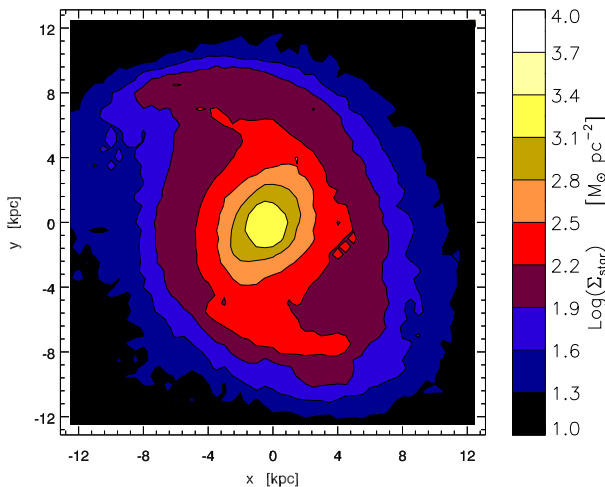


**Figure 10.** Stellar mass surface density maps (left-hand panels), Fourier amplitudes (middle panel) and phase (right-hand panel) for the GA2 galaxy at  $z = 0.55$ . Symbols and colours are like in Figs 3, 7 and 8.

takes on significant values especially at large radii, while the phase analysis reveals that the structure does not behave as a bar. So the high value of  $A_2$  is determined by the outer spiral arms more than by a central bar. This transient lasts from the first near passage of the satellite to its destruction,  $\sim 700$  Myr in total, corresponding to  $\sim 3-4$  revolutions of the disc. Then, the  $A_2$  coefficient quickly returns to  $\sim 0.1$  and keeps decreasing slowly with time.

The history of GA1 is similar. In this case, the satellite is never found at distances smaller than 20 kpc so, while the mass ratio is very similar, the tidal disturbance is smaller and the jump in  $A_2$  is much less evident.

The  $A_2$  coefficients start to grow for both galaxies after  $z = 0.2$ ,  $\sim 2$  Gyr after the minor merger has ended (i.e. after  $\sim 10$  disc revolutions). In this period, the instability grows at an accelerating pace. The growth has a markedly different time evolution with respect to the instability episode triggered by the minor merger. This suggests that the bar is due to the secular evolution of the disc. Moreover, the nice coincidence of the timing of bar growth at the two resolutions and the similar length of the resulting bar suggest that this instability is physical and not purely numerical, while the difference in bar strength is explained by the quick raise of the bar instability, so the GA1 at  $z = 0$  happens to be caught at a higher  $A_2$  value.

To investigate the physical cause of this bar instability, we consider two criteria commonly adopted in the literature to assess when a disc is unstable to bar formation. The first one, proposed by Efstathiou et al. (1982) and based on  $N$ -body simulations, predicts that the regulator of bar instability is the relative contribution of the disc to the rotation curve:

$$\Upsilon_{\text{disc}} = \frac{V_{\text{disc}}}{\sqrt{GM_{\text{disc}}/R_{\text{disc}}}}, \quad (10)$$

where,  $M_{\text{disc}}$ ,  $R_{\text{disc}}$  and  $V_{\text{disc}}$  are disc mass, radius and velocity, respectively. Bar instability takes place whenever  $\Upsilon_{\text{disc}} \leq \epsilon_{\text{lim}} \simeq 1$ . To calculate this quantity, we use for  $M_{\text{disc}}$  the mass of galaxy particles within 10 kpc and with circularities  $0.7 < \epsilon < 1.3$ , for  $R_{\text{disc}}$  the half-mass radius of the same particles and for  $V_{\text{disc}}$  the maximum of the galaxy rotation curve within 10 kpc. Results do not change if we use a different aperture to define disc mass and radius. Fig. 11 shows the quantity  $\Upsilon_{\text{disc}}$  as a function of redshift, in both cases computed either using only star particles (blue lines) or all galaxy particles (red line). As usual, the left-hand panel gives

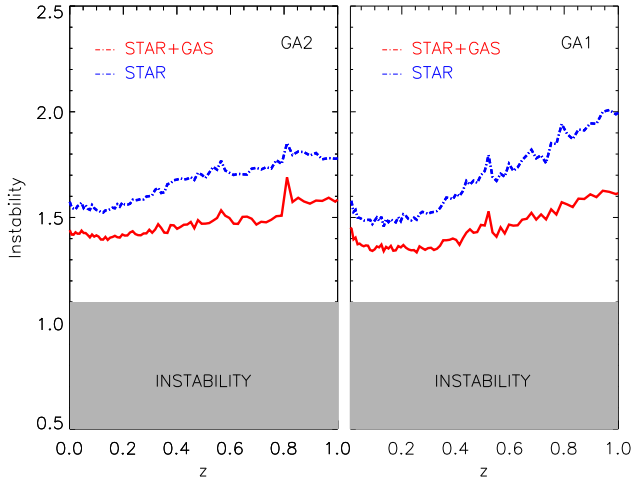


**Figure 11.**  $\Upsilon_{\text{disc}}$  as a function of redshift for star particles (dot–dashed blue line) and for all galaxy particles (continuous red line); the shaded area marks the instability region corresponding to  $\epsilon_{\text{lim}} = 1.1$ . Left-hand panel: GA2; right-hand panel: GA1.

results for GA2 and the right-hand panel for GA1. The shaded regions denote values lower than a threshold  $\epsilon_{\text{lim}} = 1.1$  (Efstathiou et al. 1982) applying to a pure stellar disc, while a lower threshold of 0.9 has been suggested to apply to gas discs. As a result, although  $\Upsilon$  decreases with time, it takes on values in any case above the suggested threshold.

The local stability of a self-gravitating disc to radial perturbations is usually evaluated using the Toomre (1964) stability criterion. Though Toomre-unstable discs are expected to fragment into self-bound knots, a mildly unstable disc may develop a bar (Julian & Toomre 1966). Furthermore, Athanassoula & Sellwood (1986) proposed that  $Q > 2$  might be a general criterion against bar formation, since for these high  $Q$  values collective density waves become very weak and growth rates of all instabilities are reduced.

To compute the Toomre parameter of a two-component disc (with gas and stars) we use, as in Monaco et al. (2012), the simplified approach of Wang & Silk (1994). This approximates well the more accurate expression recently proposed by Romeo & Wiegert (2011), provided that velocity dispersion is high, which is our case. We start from the separated component  $Q$  values:

$$Q_*(r) = \frac{\kappa \sigma_r}{3.36 G \Sigma_*} \quad (11)$$

$$Q_g(r) = \frac{\kappa \sigma_g}{3.36 G \Sigma_g}, \quad (12)$$

where, for each component,  $\Sigma(r)$  is its surface density,  $\sigma_r(r)$  its radial velocity dispersion and  $\kappa(r) = V(r)\sqrt{2 + 2d \ln V/d \ln r}/r$  the epicyclic frequency of the disc. The effective  $Q_{\text{tot}}(r)$  parameter of the disc is computed as

$$Q_{\text{tot}}(r) \simeq \left( \frac{1}{Q_g} + \frac{1}{Q_*} \right)^{-1}. \quad (13)$$

Radial velocity dispersion is computed with the  $3\sigma$  rejection method described in Section 3.1, using as stellar surface density the one obtained rejecting  $>3\sigma$  interlopers.<sup>3</sup> In all cases, we find that gas

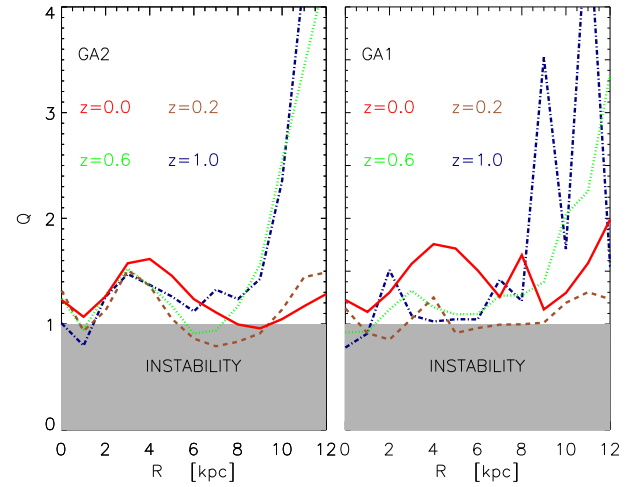


**Figure 12.** Toomre parameter  $Q_{\text{tot}}(r)$  at  $z = 0, 0.2, 0.6, 1.0$  (continuous red, dashed brown, dotted green and dot–dashed blue lines, respectively). The shaded areas show the region where disc are formally unstable. Left-hand panel: GA2; right-hand panel: GA1.

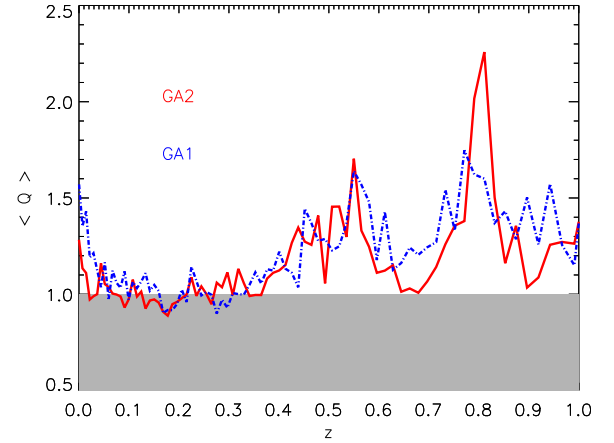


**Figure 13.** Average value of the Toomre parameter from 3 to 8 kpc, as a function of redshift, for GA1 (dot–dashed blue line) and GA2 (continuous red line). The shaded areas show the region where discs are formally unstable.

has a minor impact on  $Q_{\text{tot}}$ . In fact, using  $Q_*$  alone would lead to the same conclusions.

Fig. 12 shows  $Q_{\text{tot}}$  as a function of polar radius at redshift 0, 0.2, 0.6 and 1.0. Fig. 13 shows  $\langle Q \rangle$ , the average value of  $Q_{\text{tot}}$  in the scale range from 3 to 8 kpc, computed for all available outputs of the two simulations at  $z \leq 1$ . In these plots, the grey region denotes the  $Q < 1$  values of the Toomre parameter where the disc is expected to be unstable. These galaxies are found to be formally stable at  $z > 0.3$ , but the Toomre parameter steadily decreases with time. From Fig. 12, we see that, at  $z = 0.6$ , the disc of GA2 gets weakly unstable both at the centre and at  $\sim 6$  kpc. As  $z = 0.2$ , this second instability region has got wider, while  $\langle Q \rangle$  has got below the value of unity since  $z \sim 0.3$ . The GA1 galaxy becomes unstable at  $r \sim 2$  and 6 kpc only at  $z = 0.2$ , but the evolution of  $\langle Q \rangle$  is very similar to that of GA2. For both galaxies, the rise of the Toomre parameter at

corrections compensate in the value of  $Q_*$ , that is then very insensitive to the method used.

<sup>3</sup> We report here that, with respect to the Gaussian fit, the  $3\sigma$  rejection method yields at the same time lower  $\sigma_r$  and lower  $\Sigma_*$  (Fig. 1) and these

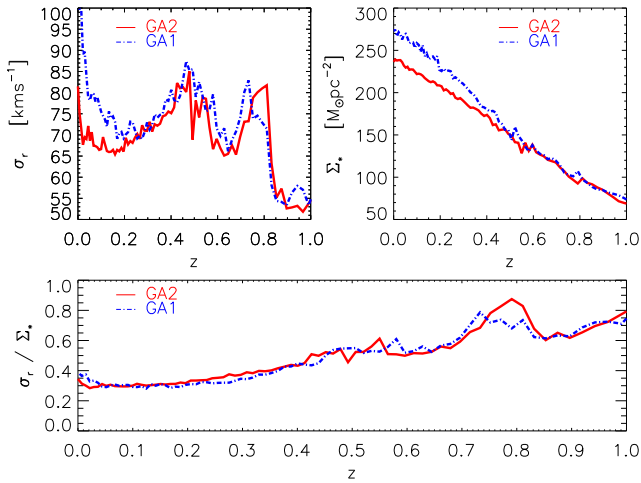


**Figure 14.** disc radial velocity dispersion (top-left panel), stellar disc surface density (top-right panel) and their ratio as a function of redshift (bottom panel). All these quantities are averaged from 3 to 8 kpc. Continuous red line for GA2 and dot-dashed blue line for GA1.

later time is due to the raise of  $\sigma_r$ , that is driven by the development of the radial streaming pattern.

Although the detailed behaviour of these galaxies is far from simple, the start of instability roughly coincides with the time when  $\langle Q \rangle$  gets lower than the canonical threshold value of 1. Hence, the behaviour of bar instability in these galaxies is consistent with the simple hypothesis that a bar is triggered by a secular instability. Assuming the validity of the criterion  $\langle Q \rangle < 1$ , the tidal disturbance at  $z = 0.55$  takes place when the disc is still stable, while disc heating due to tidal interaction leads to an increase in velocity dispersion and therefore in  $Q_{\text{tot}}$  value. This may explain why the bar-like feature of GA2 is transient.

The reason for the late-time secular decrease of  $Q_{\text{tot}}$  towards the instability region is mostly due to the accumulation of the disc mass rather than to a variation of disc velocity dispersion. In Fig. 14, we show the average disc radial velocity dispersion, stellar surface density and the ratio of the two. All quantities are evaluated in the range  $3 \leq r \leq 8$  kpc and as a function of redshift. The radial velocity dispersion (top left of Fig. 14) is boosted by the tidal interaction with the satellite and then it decreases before growing at  $z \simeq 0.1$  in both GA1 and GA2, while stellar surface densities (top right of Fig. 14) increase always with time. Accordingly, their ratio decreases with time (bottom panel of Fig. 14). This demonstrates that the decrease of  $Q_{\text{tot}}$ , that is the most likely cause of the bar, is the accumulation of the disc mass at low redshift, due to the continuous infall of gas into the DM halo.

### 3.6 The role of halo triaxiality

As mentioned in the introduction, halo triaxiality is a potential trigger of bar instability, though the precise role of triaxiality has been debated in the papers discussed above. In those papers, haloes were extracted from collisionless  $N$ -body simulations and discs were placed inside them. As a matter of fact, this implies that the gravitational influence that the formation of the disc has had on the structure of the halo itself is neglected. The impact of the formation of a gaseous disc on the shape of a DM halo and its transformation from prolate to oblate in the inner part was already studied in isolated systems by Dubinski (1994), Debattista et al. (2008), in cosmological environment by Kazantzidis et al. (2004),

Tissera et al. (2010), Abadi et al. (2010) and more recently by Zemp et al. (2012) and Bryan et al. (2013). DeBuhr, Ma & White (2012) inserted live stellar discs inside Milky Way-like DM haloes from the Aquarius simulations, finding a strong effect on the shapes of the inner haloes which evolve to become oblate.

In our Paper I, we have shown that, consistently with many other papers (e.g. Governato et al. 2012), the inner slope of the DM halo of our GA2 simulation is flatter than the typical  $\rho \propto r^{-1}$  slope obtained when particles are collisionless. This is due to the combined action of the adiabatic contraction caused by the formation of the galaxy and the violent expansion due to episodic massive outflows. The same process induces changes in the DM distribution in the region occupied by the galaxy.

To address the influence that the formation of the galaxy has on the inner regions of the DM halo, we performed a simulation of the GA2 switching off hydrodynamics, cooling and star formation, thus treating both DM and gas particles as collisionless particles; we will call it GA2-class in the following. For the GA2 and GA2-class simulations, we compute the inertia tensor of all DM particles within a distance of  $r_{200}/10$  (30.64 kpc for GA2-class, 29.98 kpc for GA2) and quantify the ratios among the eigenvalues  $I_i$  (with  $i = 1, 2, 3$ ), ranked in decreasing order. In GA2-class, we find  $I_1/I_2 = 1.07$ ,  $I_1/I_3 = 1.39$  and  $I_2/I_3 = 1.30$ , indicating a roughly prolate shape with significant triaxiality. In GA2, where the DM halo has hosted a forming spiral galaxy, the ratios of eigenvalues are  $I_1/I_2 = 1.13$ ,  $I_1/I_3 = 1.14$  and  $I_2/I_3 = 1.01$ , indicating an oblate and nearly axisymmetric shape. Moreover, the eigenvector corresponding to the largest eigenvalue of the inertia tensor, i.e. to the direction where the halo is flattened, is found to be aligned with the galaxy angular momentum within  $4.37^\circ$ . This alignment allows us to infer that the oblate shape is due to the formation of the disc itself.

We conclude that the influence of the triaxiality on disc dynamics should not be addressed without considering, at the same time, the influence that astrophysical processes bringing to disc formation have on the triaxiality of the inner part of the DM halo.

## 4 THE AQ5 AND AQ6 GALAXIES

The two AqC simulations show a different behaviour with respect to the GA ones. Here, we show the surface density maps (Fig. 15), the face-on map of radial velocities (Fig. 16), the Fourier coefficients and phases (Fig. 17) and the evolution of  $A_2$  and  $\langle Q \rangle$ , the latter being averaged again on  $3 < r < 8$  kpc (Fig. 18). The higher resolution AqC5 galaxy at  $z = 0$  has a bar with properties similar to the one of GA2 (Fig. 15), visible as an elongation of the isodensity contours, but with a slightly smaller size with respect to the GA galaxies (Fig. 15). The signature of streaming motions very clearly confirms the visual impression (Fig. 16). The Fourier analysis (Fig. 17) confirms the presence of a bar with maximal amplitude of  $C_2/C_0 \sim 0.5$  at  $\sim 4$  kpc and a bar length of  $L_{\text{bar}} = 6.3$  kpc. Spiral arms here give a much smaller contribution to the amplitude of the  $m = 2$  mode.

The origin of this bar is however different: in Fig. 18, we see that the  $A_2$  coefficient starts to increase at  $z \sim 0.6$ , while the disc is stable according to  $\langle Q \rangle$ . As mentioned in Section 2, this galaxy happens to suffer a minor merger at roughly the same time as the GA galaxy. In particular, at  $z = 0.52$ , the galaxy suffers a near passage at  $\sim 20$  kpc of a  $1.6 \times 10^9 M_\odot$  satellite, with a mass ratio of 1:32 with respect to the main galaxy. Further near passages are at  $z = 0.43$  and  $0.35$ , when the satellite gets tidally destroyed. These times are reported in Fig. 18 as vertical black lines. This coincides with the time interval where the  $A_2$  coefficient increases from  $\sim 0.05$

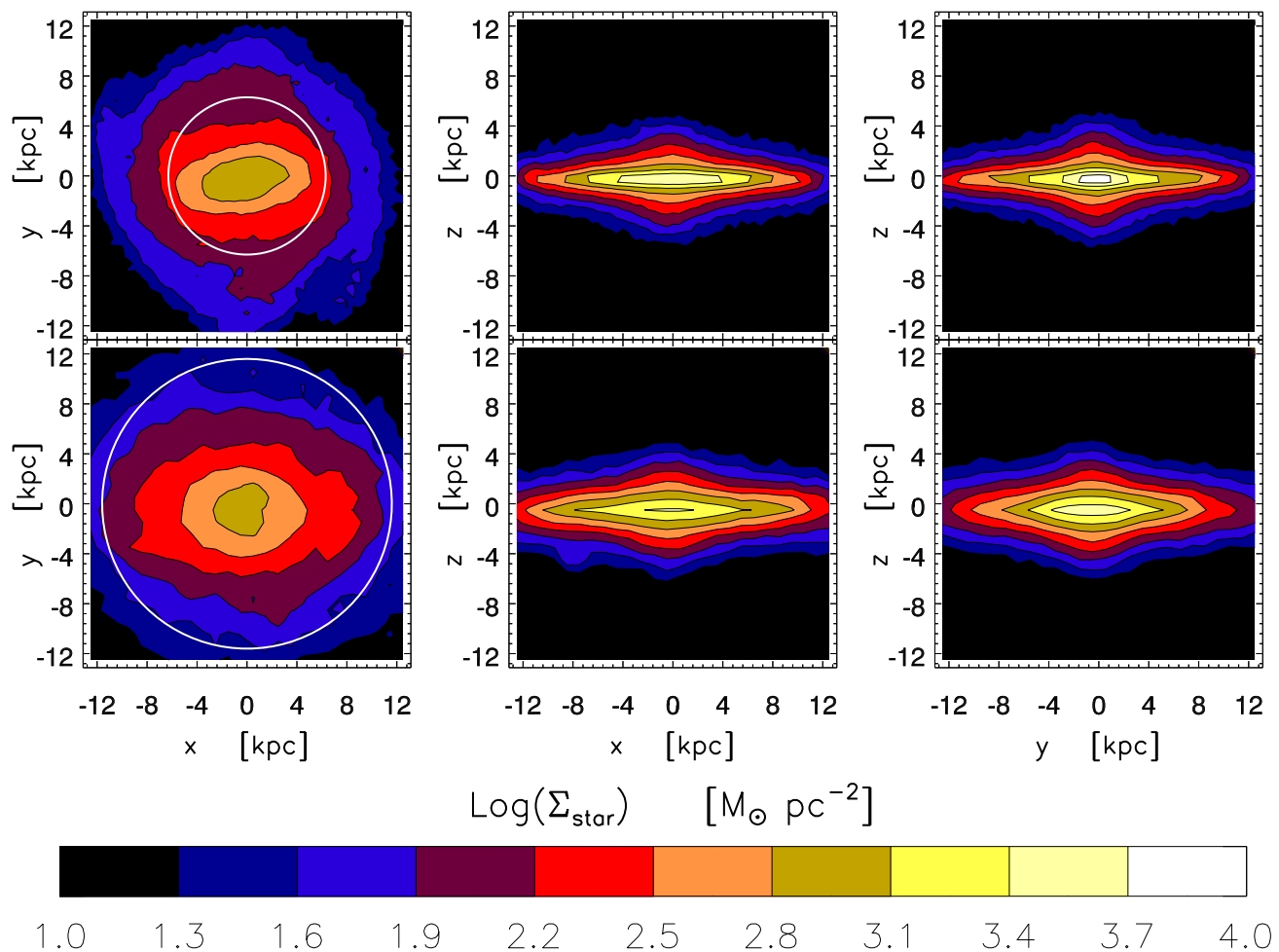


**Figure 15.** As in Fig. 3: projected stellar maps of the AqC5 (top panels) and AqC6 (bottom panels) galaxies at  $z = 0$ . The white circle marks the bar length  $L_{\text{bar}}$ .

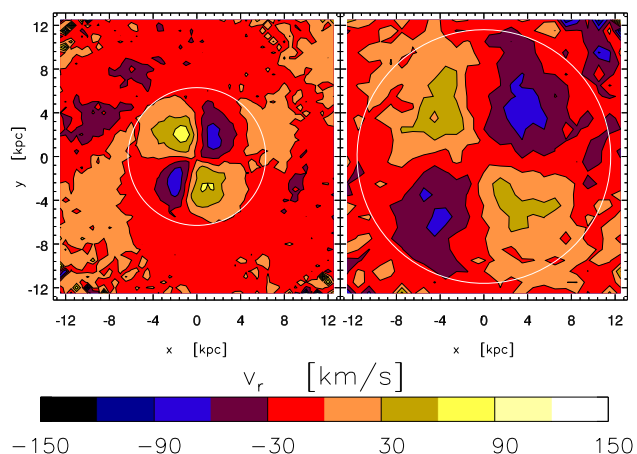


**Figure 16.** As in Fig. 6: radial velocity maps on edge-on views of the two simulated AqC5 (left-hand panel) and AqC6 (right-hand panel) galaxies. The white circle marks the bar length  $L_{\text{bar}}$ .

to  $\sim 0.17$  and it supports the idea that this bar is triggered by a tidal interaction. The main difference with respect to the GA galaxy lies in the higher mass ratio, though the merger is still considered minor.

The AqC6 galaxy behaves differently. Analogously to the GA simulations, the perturbation from the satellite does not trigger a

bar. Indeed, the dynamics of the merger is different in this case: the satellite suffers a much slower orbital decay, so that the apocentre of the orbit is still  $\sim 30$  kpc at  $z = 0.45$ . The nearest encounter, at 19 kpc, is found only at  $z = 0.24$ , while the tidal disruption takes place at  $z = 0.14$ . At such late times, the  $Q_{\text{tot}}$  parameter is close to 1 and the  $A_2$  coefficient starts to raise again as in the GA case. While the cause in this case seems to be the disc secular evolution (driven by the progressive accumulation of the disc mass, as in Fig. 14), we cannot exclude that the bar is tidally triggered.

Figs 15–17 show that in this case the bar-like signatures in streaming motions and Fourier analysis are relatively strong, but the bar is very long, with an estimated length of  $L_{\text{bar}} = 11$  kpc and the isodensity contours are not very flattened. The galaxy appears to be caught during the early development of a very strong and long bar.

## 5 CONCLUSIONS

In Paper I, we showed results of simulations of disc galaxies in  $\sim 2\text{--}3 \times 10^{12} M_{\odot}$  haloes, using two sets of ICs (GA, Stoehr et al. 2002 and AqC, Springel et al. 2008, Scannapieco et al. 2009) at two resolutions. In all cases, extended discs were obtained with low  $B/T$  ratios and general properties (disc size, mass surface density, rotation velocity, gas fraction) that are consistent with observations of the local Universe. These galaxies develop a bar at low redshift, which is still consistent with the relatively high fraction

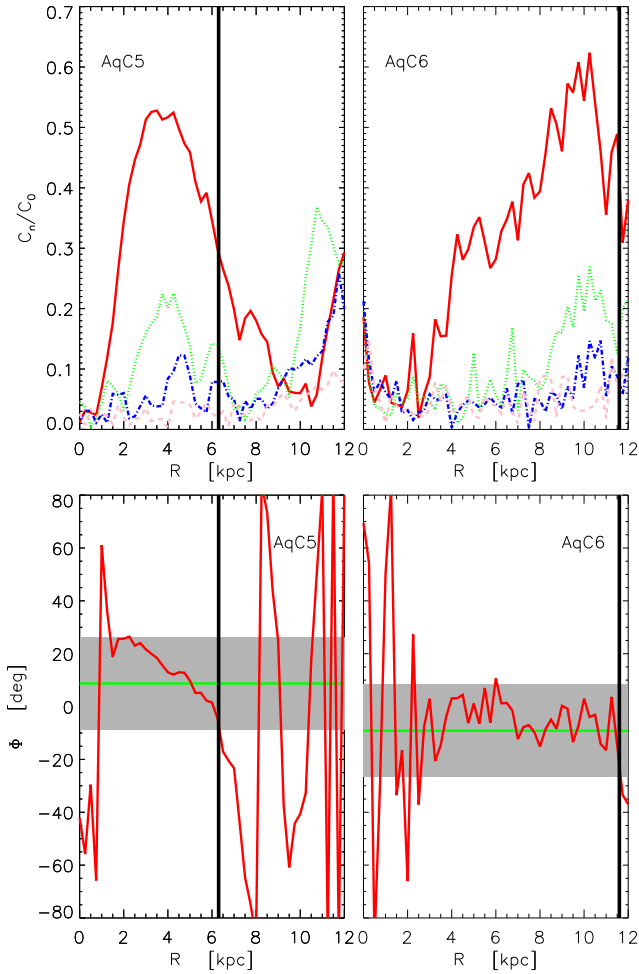


**Figure 17.** As in Figs 7 and 8: Fourier analysis of the AqC5 (left-hand panels) and AqC6 (right-hand panels) galaxies. Upper panels show the amplitude of even Fourier coefficients, the lower panels the phase of  $C_2$ . The black lines mark the bar length  $L_{\text{bar}}$ .

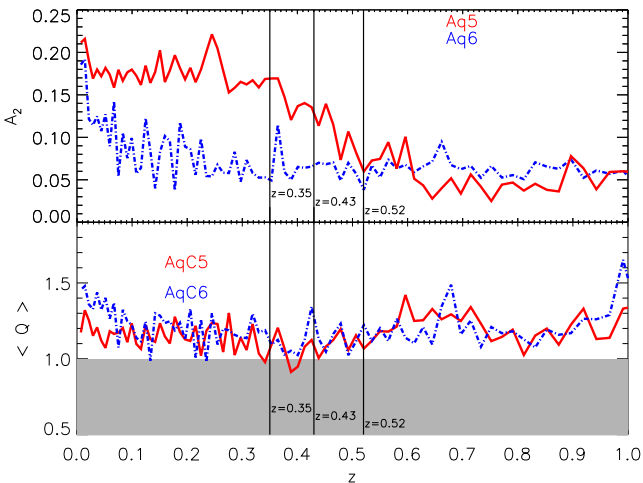


**Figure 18.** As in Figs 9 and 13: evolution with redshift of  $A_2$  (upper panel) and  $\langle Q \rangle$  (lower panel) for the AqC5 (continuous red lines) and AqC6 (dot-dashed blue lines). Vertical lines give the times of near passages and final merger of the satellite.

( $\sim 60$  per cent) of bars found in such massive spiral galaxies. In this paper, we quantified the properties of these bars, starting from morphology and kinematics of the inner region of the galaxies, and then performing a Fourier analysis of the mass surface density map to assess the strength and length of the bars. We investigated the physical conditions that cause bar instability and found that a combination of low values of Toomre parameters and minor mergers can explain the emergence of bars in our simulations.

Our main conclusions are the following.

(i) The close similarity of bar properties at  $z = 0$  and of the development of the instability at  $z \leq 0.3$  for GA2 and GA1, which differ in mass resolution by a factor of 9.3, disfavours the hypothesis that these bars are a result of a numerical instability due to poor resolution.

(ii) Despite the softening does not allow us to properly resolve the vertical structure of the disc, we find our simulated discs to have vertical and radial velocity dispersion compatible with observations, at least for  $r < 10$  kpc.

(iii) In the GA simulations, the morphology and kinematics of the inner  $\sim 10$  kpc are fully consistent with the presence of a bar. In both cases, the typical kinematic signatures of increased line-of-sight velocity dispersion and radial streaming motions are present. The Fourier analysis shows that  $C_2/C_0$  peaks to values of 0.4 and 0.7 in the GA2 and GA1 cases, that the bar length is  $L_{\text{bar}} \simeq 8.8$  kpc in both cases.

(iv) The time evolution of  $A_2$  shows that this instability starts at  $z = 0.2$  and quickly rises at  $z = 0$  for both GA2 and GA1, so the difference in bar strength is likely due to a small time offset in the growth of the structure.

(v) Before the onset of bar instability, discs result to be stable according to the criterion proposed by Efstathiou et al. (1982) and they are very close to the threshold of Toomre instability, with  $Q_{\text{tot}} \simeq 1$ .

(vi) A minor merger taking place from  $z = 0.57$  to 0.35, with a stellar mass ratio of 1: 50, results, especially in GA2, in a transient tidal disturbance with high values of the  $A_2$  coefficient which disappears as quickly as it has appeared. A Fourier analysis reveals that the perturbation is due to a strong spiral pattern rather than to a bar.

(vii) The AqC simulations follow a different path. At a higher resolution (AqC5), a minor merger taking place from  $z = 0.52$  to 0.35 induces a true bar that lasts until the end of the simulation. The  $\langle Q \rangle$  parameter is greater than 1 before the first close encounter with the satellite, but the mass ratio is higher in this case (1: 32) and this likely justifies the different behaviour of AqC5 with respect to GA2. The final bar has a length of  $L_{\text{bar}} = 6.5$  kpc.

(viii) The minor merger in AqC6 takes place at later times. In this case, the disc gets barred in a way similar to the GA galaxy. However, in this case the role of the merger in the triggering of the bar cannot be excluded. The resulting bar is very long ( $L_{\text{bar}} = 11$  kpc) and it is caught in a relatively early phase of development.

(ix) We find that the formation of the disc influences the triaxiality of the inner regions of the DM halo. In the GA2-class simulation, performed treating both DM and gas particles as collisionless particles, the DM halo is triaxial, while in GA2, where the halo has hosted the formation of a spiral galaxy, the inertia tensor of the DM halo is roughly oblate and its eigenvector corresponding to the largest eigenvalue is found to be well aligned with the galaxy angular momentum. Thus, special care is needed in addressing the role of triaxiality on bar instability when discs are embedded in DM haloes extracted from collisionless simulations.

Overall, our simulations are consistent with a relatively simple picture of bar instability being triggered either by secular processes in Toomre-unstable discs ( $Q_{\text{tot}} \lesssim 1$ ) or by minor mergers, when the stellar mass ratio is at least of the order of 1:30. With mass ratios as small as 1:50, the merger can stimulate transient features that may look like bars but do not pass a test based on Fourier phases. Of course, these simulations do not give sufficient statistics to provide this picture with the proper justification. We tested several versions of our code on these sets of IC and we noticed that bars may or may not come out, depending on the detailed state of the galaxy. For instance, the AqC5 galaxy in the Scannapieco et al. (2012) paper, run with a previous version of our code with pure thermal feedback, primordial cooling and no chemical evolution, showed a very strong bar (the whole disc had collapsed into a cigar-like structure). A similar thing happens to GA2 when simulated with the same code. In this two cases, we found that the bar is triggered by the two minor mergers discussed above, while the discs are Toomre stable before the merger. The difference in this case is that, due to the fact that feedback is less effective in limiting star formation in small haloes, mass ratios are much larger.

As a concluding remark, our results are found to be stable with resolution at least in the GA case; hence, we consider the origin of the bar physical rather than purely numerical. However, the presence of a bar depends on the fine details of the disc structure and its environment that are not yet numerically under full control, as the different timing of the satellite merging in AqC5 and AqC6 testifies. So these results are not a premise to a robust prediction of the presence of bars in simulated discs, but it will certainly allow us to better understand the emergence of this complex phenomenon that, although it has been observed since the beginning of extragalactic astronomy, is still not well understood.

## ACKNOWLEDGEMENTS

We thank Volker Springel who provided us with the non-public version of the GADGET-3 code. We acknowledge useful discussions with Stefano Borgani, Gabriella De Lucia, Emiliano Munari and Marianna Annunziatella. The simulations were carried out at the ‘Centro Interuniversitario del Nord-Est per il Calcolo Elettronico’ (CINECA, Bologna), with CPU time assigned under University-of-Trieste/CINECA and IS CRA grants, and at the CASPUR computing centre with CPU time assigned under two standard grants. This work is supported by the PRIN MIUR 2010-2011 grant ‘The dark Universe and the cosmic evolution of baryons: from current surveys to Euclid’, by the PRIN-MIUR 2012 grant ‘Evolution of Cosmic Baryons’, by the PRIN-INAF 2012 grant ‘The Universe in a Box: Multi-scale Simulations of Cosmic Structures’, by the INFN ‘INDARK’ grant, by the European Com- missions FP7 Marie Curie Initial Training Network CosmoComp (PITN-GA-2009-238356), by the FRA2012 grant of the University of Trieste and by ‘Consorzio per la Fisica di Trieste’.

## REFERENCES

Abadi M. G., Navarro J. F., Steinmetz M., Eke V. R., 2003, *ApJ*, 597, 21  
 Abadi M. G., Navarro J. F., Fardal M., Babul A., Steinmetz M., 2010, *MNRAS*, 407, 435  
 Aguerri J. A. L., Beckman J. E., Prieto M., 1998, *AJ*, 116, 2136  
 Aguerri J. A. L., Debattista V. P., Corsini E. M., 2003, *MNRAS*, 338, 465  
 Athanassoula E., 2005, *MNRAS*, 358, 1477  
 Athanassoula E., Misiriotis A., 2002, *MNRAS*, 330, 35  
 Athanassoula E., Sellwood J. A., 1986, *MNRAS*, 221, 213

Athanassoula E., Machado R. E. G., Rodionov S. A., 2013, *MNRAS*, 429, 1949  
 Aumer M., White S. D. M., Naab T., Scannapieco C., 2013, *MNRAS*, 434, 3142  
 Barazza F. D., Jogee S., Marinova I., 2008, *ApJ*, 675, 1194  
 Berentzen I., Shlosman I., Jogee S., 2006, *ApJ*, 637, 582  
 Bosma A., 1978, PhD thesis, Univ. Groningen  
 Bryan S. E., Kay S. T., Duffy A. R., Schaye J., Dalla Vecchia C., Booth C. M., 2013, *MNRAS*, 429, 3316  
 Buta R., Laurikainen E., Salo H., Block D. L., Knapen J. H., 2006, *AJ*, 132, 1859  
 Combes F., Elmegreen B. G., 1993, *A&A*, 271, 391  
 Curir A., Mazzei P., 1999, *A&A*, 352, 103  
 Curir A., Mazzei P., Murante G., 2006, *A&A*, 447, 453  
 Curir A., Mazzei P., Murante G., 2007, *A&A*, 467, 509  
 Curir A., Mazzei P., Murante G., 2008, *A&A*, 481, 651  
 Debattista V. P., Sellwood J. A., 1996, preprint ([arXiv:e-prints](https://arxiv.org/abs/199605001))  
 Debattista V. P., Sellwood J. A., 2000, *ApJ*, 543, 704  
 Debattista V. P., Mayer L., Carollo C. M., Moore B., Wadsley J., Quinn T., 2006, *ApJ*, 645, 209  
 Debattista V. P., Moore B., Quinn T., Kazantzidis S., Maas R., Mayer L., Read J., Stadel J., 2008, *ApJ*, 681, 1076  
 DeBuhr J., Ma C.-P., White S. D. M., 2012, *MNRAS*, 426, 983  
 Dubinski J., 1994, *ApJ*, 431, 617  
 Dubinski J., Gauthier J.-R., Widrow L., Nickerson S., 2008, in Funes J. G., Corsini E. M., eds, *ASP Conf. Ser. Vol. 396, Formation and Evolution of Galaxy Disks*. Astron. Soc. Pac., San Francisco, p. 321  
 Efstathiou G., Lake G., Negroponte J., 1982, *MNRAS*, 199, 1069  
 Elmegreen B. G., Elmegreen D. M., 1985, *ApJ*, 288, 438  
 Eskridge P. B. et al., 2000, *AJ*, 119, 536  
 Fall S. M., Efstathiou G., 1980, *MNRAS*, 193, 189  
 Gadotti D. A., 2011, *MNRAS*, 415, 3308  
 Governato F., Willman B., Mayer L., Brooks A., Stinson G., Valenzuela O., Wadsley J., Quinn T., 2007, *MNRAS*, 374, 1479  
 Governato F. et al., 2012, *MNRAS*, 422, 1231  
 Guedes J., Callegari S., Madau P., Mayer L., 2011, *ApJ*, 742, 76  
 Guedes J., Mayer L., Carollo M., Madau P., 2013, *ApJ*, 772, 36  
 Julian W. H., Toomre A., 1966, *ApJ*, 146, 810  
 Kazantzidis S., Kravtsov A. V., Zentner A. R., Allgood B., Nagai D., Moore B., 2004, *ApJ*, 611, L73  
 Kormendy J., 1982, *ApJ*, 257, 75  
 Kormendy J., Kennicutt R. C., Jr, 2004, *ARA&A*, 42, 603  
 Kraljic K., Bournaud F., Martig M., 2012, *ApJ*, 757, 60  
 Leroy A. K., Walter F., Brinks E., Bigiel F., de Blok W. J. G., Madore B., Thornley M. D., 2008, *AJ*, 136, 2782  
 Marinacci F., Pakmor R., Springel V., 2013, *MNRAS*  
 Michel-Dansac L., Wozniak H., 2006, *A&A*, 452, 97  
 Monaco P., Murante G., Borgani S., Dolag K., 2012, *MNRAS*, 421, 2485  
 Murante G., Monaco P., Giovalini M., Borgani S., Diaferio A., 2010, *MNRAS*, 405, 1491  
 Murante G., Monaco P., Borgani S., Tornatore L., Dolag K., Goz D., 2015, *MNRAS*, 447, 178 (Paper I)  
 Navarro J. F., Frenk C. S., White S. D. M., 1996, *ApJ*, 462, 563  
 Noguchi M., 1996, *ApJ*, 469, 605  
 Ohta K., 1996, in Buta R., Crocker D. A., Elmegreen B. G., eds, *ASP conf. Ser. Vol. 91, IAU Colloq. 157: Barred Galaxies*. Astron. Soc. Pac., San Francisco, p. 37  
 Ohta K., Hamabe M., Wakamatsu K.-I., 1990, *ApJ*, 357, 71  
 Okamoto T., 2013, *MNRAS*, 428, 718  
 Okamoto T., Isoe M., Habe A., 2014, preprint ([arXiv:e-prints](https://arxiv.org/abs/1405.0001))  
 Ostriker J. P., Peebles P. J. E., 1973, *ApJ*, 186, 467  
 Romeo A. B., Wiegert J., 2011, *MNRAS*, 416, 1191  
 Scannapieco C., Athanassoula E., 2012, *MNRAS*, 425, L10  
 Scannapieco C., Tissera P. B., White S. D. M., Springel V., 2006, *MNRAS*, 371, 1125  
 Scannapieco C., Tissera P. B., White S. D. M., Springel V., 2008, *MNRAS*, 389, 1137

- Scannapieco C., White S. D. M., Springel V., Tissera P. B., 2009, *MNRAS*, 396, 696
- Scannapieco C. et al., 2012, *MNRAS*, 423, 1726
- Sellwood J. A., Nelson R. W., Tremaine S., 1998, *ApJ*, 506, 590
- Springel V., 2005, *MNRAS*, 364, 1105
- Springel V., White S. D. M., Tormen G., Kauffmann G., 2001, *MNRAS*, 328, 726
- Springel V. et al., 2008, *MNRAS*, 391, 1685
- Stinson G. S. et al., 2013, *MNRAS*, 436, 625
- Stoehr F., White S. D. M., Tormen G., Springel V., 2002, *MNRAS*, 335, L84
- Teyssier R., 2002, *A&A*, 385, 337
- Tissera P. B., White S. D. M., Pedrosa S., Scannapieco C., 2010, *MNRAS*, 406, 922
- Toomre A., 1964, *ApJ*, 139, 1217
- Tornatore L., Borgani S., Dolag K., Matteucci F., 2007, *MNRAS*, 382, 1050
- Wang B., Silk J., 1994, *ApJ*, 427, 759
- White S. D. M., Rees M. J., 1978, *MNRAS*, 183, 341
- Wiersma R. P. C., Schaye J., Theuns T., Dalla Vecchia C., Tornatore L., 2009, *MNRAS*, 399, 574
- Zemp M., Gnedin O. Y., Gnedin N. Y., Kravtsov A. V., 2012, *ApJ*, 748, 54

This paper has been typeset from a  $\text{\TeX}/\text{\LaTeX}$  file prepared by the author.